Supporting Information for

Liquid-liquid interface-promoted formation of a porous molecular crystal based on a luminescent platinum(II) complex

Mari Kimura, Masaki Yoshida,* Sho Fujii, Atsushi Miura, Kosei Ueno, Yasuhiro Shigeta,† Atsushi Kobayashi, and Masako Kato*

Department of Chemistry, Faculty of Science, Hokkaido University, North-10 West-8, Kita-ku, Sapporo, Hokkaido 060-0810, Japan.
†Current address: Nanomaterials Research Institute, Kanazawa University, Kakuma-machi, Kanazawa, Ishikawa 920-1192, Japan.

E-mail: myoshida@sci.hokudai.ac.jp, mkato@sci.hokudai.ac.jp

Table of Contents

Experimental Details

References

Experimental Details

Materials

Caution! *Although we experienced no difficulties, all the chemicals used in this study are potentially harmful and should be used in small quantities and handled with care in a fume hood.* 2-Phenylbenzimidazole (Hpbim) and Span 20 were purchased from Tokyo Chemical Industry Co., Ltd. Picolinic acid (Hpic), Na_2CO_3, and liquid paraffin were purchased from FUJIFILM Wako Pure Chemical Co. Pluronic F-127 was purchased from Aldrich Chemical Co., Inc. All solvents were purchased from Kanto Chemical Co., Inc. *Cis*-[$PtCl_2(DMSO)_2$] (DMSO = dimethyl sulfoxide) was synthesised according to the literature method.[S1]

Synthesis of [Pt(pbim)Cl(DMSO)]: A mixture of *cis*-[$PtCl_2(DMSO)_2$] (200 mg, 0.44 mmol) and Hpbim (92.1 mg, 0.47 mmol) in degassed methanol (20 mL) was sealed in a pressure-resistant vial and heated at 393 K for 9 h. After cooling to room temperature, the vial was opened and the reaction mixture was filtered to remove insoluble materials. The filtrate was evaporated to dryness and recrystallised from DMSO/H_2O. The pale yellow residue was purified with silica-gel column chromatography (eluent: $CHCl_3$/ethyl acetate = 1/5 (v/v); R_f = 0.76), and recrystallised again from DMSO/H_2O to afford the target compound as a pale yellow powder. Yield, 83.8 mg (0.17 mmol, 38%). ^{1}H NMR (DMSO-d_6, 400 MHz): δ = 8.83 (d, J = 7.8 Hz, 1H), 8.27 (dd, J = 7.8, 1.2 Hz, 1H), 7.72 (dd, J = 7.3, 1.4 Hz, 1H), 7.59 (d, J = 7.7 Hz, 1H), 7.33-7.14 (m, 4H), 2.54 (s, 6H).

Synthesis of [Pt(pbim)(pic)] (1): A mixture containing [Pt(pbim)Cl(DMSO)] (351 mg, 0.70 mmol), Hpic (103 mg, 0.84 mmol) and Na_2CO_3 (371 mg, 3.5 mmol) in degassed acetonitrile (15 mL) was heated to reflux for 16 h under an N_2 atmosphere. The reaction mixture was cooled to room temperature, and the yellow precipitate was collected by filtration and washed with acetonitrile and water to afford the target compound as a yellow powder. Yield, 206 mg (0.40 mmol, 58%). ^{1}H NMR (DMSO-d_6, 400 MHz): δ = 9.30 (d, J = 5.4 Hz, 1H), 8.38 (td, J = 1.2, 7.6 Hz, 1H), 8.28 (m, 1H), 8.05 (dd, J = 1.3, 7.7 Hz, 1H), 7.89 (td, J = 1.8, 6.7 Hz, 1H), 7.73 (m, 1H), 7.62 (dd, J = 1.7, 7.3 Hz, 2H), 7.37 (m, 2H), 7.22 (m, 2H). Anal. calc. for $C_{19}H_{13}N_3O_2Pt \cdot 0.65H_2O$: C, 43.71; H, 2.76; N, 8.05%. Found: C, 43.33; H, 2.37; N, 7.95%. The PXRD analysis revealed that this as-synthesised form of **1** consists of the pure nonporous form **1N** (Fig. 2(a)).

Crystallisation

1N: A solution of **1** (0.125 mM) in 2 mL of a MeOH/H_2O (v/v = 1/1) mixture was stored at 4 °C for 1 week. Yellow crystals of **1N** suitable for X-ray crystallography were obtained (entry 1 in Table S1).

1P by typical crystallization method: Diethyl ether vapour was slowly diffused into a methanolic solution of **1** (0.5 mM, 3 mL) at 10 °C for 1 week. Orange crystals of **1P** suitable for X-ray

crystallography were obtained, along with the yellow powder of **1N** (entry 2 in Table S1).

1P crystallised using emulsion (general method for screening): A solution containing **1** (0.25 mM) and surfactant (0.2 mM; Pluronic F-127 or Span 20) in MeOH (1 mL) was filtered through a membrane filter, added to 1 mL of alkane (typically, cyclohexane; see Table S5), then sonicated for 1 min (Branson B-42 (44 kHz, 180 W)). Water (1 mL) was then immediately added to this mixture and it was sonicated again for 1 min to generate an emulsion of cyclohexane in the MeOH/H_2O (v/v = 1/1) mixture (final concentrations: [**1**] = 0.125 mM, [surfactant] = 0.1 mM). This mixture was allowed to stand at 10 °C and orange crystals of **1P** were obtained after a few days. The SXRD analysis of the cyclohexane-included **1P** crystal was performed with a crystal prepared by using cyclohexane dispersion with Span 20.

1P crystallised using emulsion (large-scale synthesis): A solution containing **1** (0.25 mM) and Pluronic F-127 (0.2 mM) in MeOH (1 mL) was filtered through a membrane filter, added to 1 mL of cyclohexane, then sonicated for 1 min (Branson B-42 (44 kHz, 180 W) or Branson M2800-J (40 kHz, 110 W)). Water (1 mL) was then immediately added to this mixture and it was sonicated again for 1 min to generate an emulsion of cyclohexane in the MeOH/H_2O (v/v = 1/1) mixture (final concentrations: [**1**] = 0.125 mM, [Pluronic F-127] = 0.1 mM). This emulsion was then added to a solution of **1** (0.125 mM) in 30 mL of a MeOH/H_2O (v/v = 1/1) mixture in a 50 mL vial. This vial was sealed and gently shaken twice. Orange crystals of **1P** were obtained after 1 day at 26 °C. The yield from 13 vials was 16.4 mg (0.028 mmol, 54%). The PXRD pattern for the orange crystals was identical to the simulated pattern for **1P**, and no peaks assignable to **1N** were observed (Fig. 2(a)). The ^{1}H NMR and the thermogravimetric analysis indicated the presence of included cyclohexane molecules (Fig. S6(a,b)).

Measurements

Single Crystal X-ray Diffraction (SXRD)

SXRD measurements were performed using a Rigaku XtaLAB-Synergy diffractometer with a HyPix-6000HE area detector and a multilayer mirror-monochromated Cu K_α radiation (λ = 1.54184 Å). Each crystal was mounted on a MicroMount using Paratone-N oil, and cooled using a N_2-flow type temperature controller. Diffraction data were collected and processed using *CrysAlisPro*.[S2] The structures were solved using *SHELXT-2014*[S3] by the intrinsic phasing method. Structure refinements were conducted by the full-matrix least squares techniques with *SHELXL-2017*.[S4] For paraffin-included crystals (**1P**•Paraffin), the diffused electron densities resulting from residual solvent molecules were removed from the data set using the *SQUEEZE* routine[S5a] of *PLATON*[S5b] and refined further using the data generated. All non-hydrogen atoms were refined anisotropically, and hydrogen atoms were refined using the riding model. The crystallographic data are summarised in

Table S7 and have been deposited to the Cambridge Crystallographic Data Centre (CCDC 2003915-2003918 and 2032282).

Powder X-ray Diffraction (PXRD)

PXRD measurements were conducted using Cu K_α radiation (λ = 1.5418 Å) on a Bruker D8 Advance diffractometer equipped with a graphite monochromator and a one-dimensional LinxEye detector, or a Rigaku SPD diffractometer at the BL-8B beamline (λ = 1.5455 Å) of the Photon Factory, Japan.

Optical Microscopy and Microspectroscopy

To observe the crystallisation of **1P** at the liquid-liquid interface, a solution of **1** (15 μL, 0.125 mM) in a MeOH/H_2O (v/v = 1/1) mixture was slowly layered onto liquid paraffin on the microscope slide (TOSHIN RIKO). The crystallisation was then monitored using an inverted optical microscope (OLYMPUS, IX71) equipped with a CMOS camera (WRAYMER, WRAYCAM-VEX120) and a 100 W halogen lamp (OLYMPUS, U-LH100).

To record the emission spectra and the emission lifetimes of crystals of **1P** formed in situ, an emulsion of cyclohexane in a MeOH/H_2O (v/v = 1/1) mixture containing **1** and Pluronic F-127 (see above "**1P** crystallised using emulsion" for details) was introduced to the analysis chamber mounted on an inverted optical microscope (OLYMPUS, IX71) equipped with a CCD camera (JAI, CV-53200). A picosecond pulsed laser beam (Becker & Hickl, BDL-488-c; λ = 488 nm, repetition rate = 20 MHz) was introduced into the microscope through an objective lens (×40, N.A. = 0.60). Emission spectra were measured for crystals of **1P** formed in situ with a multichannel photodetector (Hamamatsu Photonics, PMA-12 C10027). Emission decay profiles were measured for the crystals of **1P** formed in situ with the use of an avalanche photodiode (MPD, SPAD-050-CTD), and analysed with a time correlated single photon counting (TCSPC) module (Becker & Hickl, SPC-130-EMN). Emission decay curves were analysed with a non-linear least squares iterative convolution method based on the Levenberg-Marquardt algorithm.[S6]

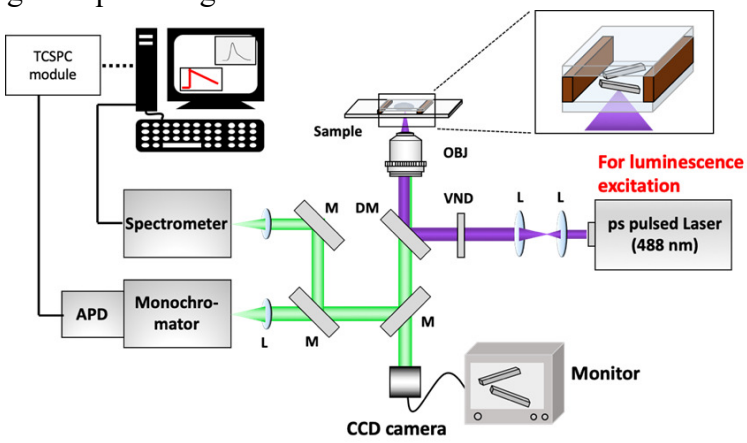

Scheme S1. Schematic illustration of the microspectroscopic imaging system (L: lens; M: mirror; DM: dichroic mirror; VND: variable neutral density filter; OBJ: objective lens; APD: avalanche photodiode).

All other microscopic observations were conducted using a KEYENCE VHX-600 digital microscope.

Photophysical Measurements

UV-vis absorption spectra were recorded on Shimadzu UV-2500PC spectrophotometer. UV-vis diffuse-reflectance spectra were recorded using the same spectrophotometer equipped with an integrating sphere accessory. The solid samples were diluted by MgO, and the measured reflectivity was converted by the Kubelka-Munk function. Emission spectra were recorded on a JASCO FP-8600 spectrofluorometer. Luminescence quantum yields were recorded on a Hamamatsu Photonics C9920-02 absolute photoluminescence quantum yield measurement system equipped with an integrating sphere apparatus and a 150 W CW xenon light source. The accuracy of the instrument was confirmed based on a measurement of the quantum yield of anthracene in ethanol (Φ = 0.27).[S7] The emission lifetime measurements were conducted using a Hamamatsu Photonics C4780 system equipped with a Hamamatsu Photonics C4334 streak camera as a photodetector and an Usho KEN-X nitrogen laser for the 337 nm excitation. Liquid N_2 cryostat (Optistat-DN optical Dewar and ITC-503 temperature controller, Oxford Instruments) was used for the temperature control.

Other Measurements

^{1}H NMR spectra were acquired on a JEOL JNM-ECZ-400S spectrometer. Thermogravimetric (TG) analysis was performed using a Rigaku Thermoplus EVO TG-DTA 8120 with Al sample pans under an Ar flow. Elemental analysis was conducted at the Analysis Centre of Hokkaido University.

Computational Methods

The time-dependent DFT (TDDFT) calculation was performed with the PBE1PBE-D3[S8] functional as implemented in the Gaussian09 program.[S9] The SDD[S10] basis set and associated effective core potential were used for Pt. The 6-311G(d,p) basis set was employed for all other atoms.[S11] Structure of trimeric unit of **1P** was taken from the single-crystal X-ray data of **1P** without optimisation. The calculated vertical excitations were listed in Table S8.

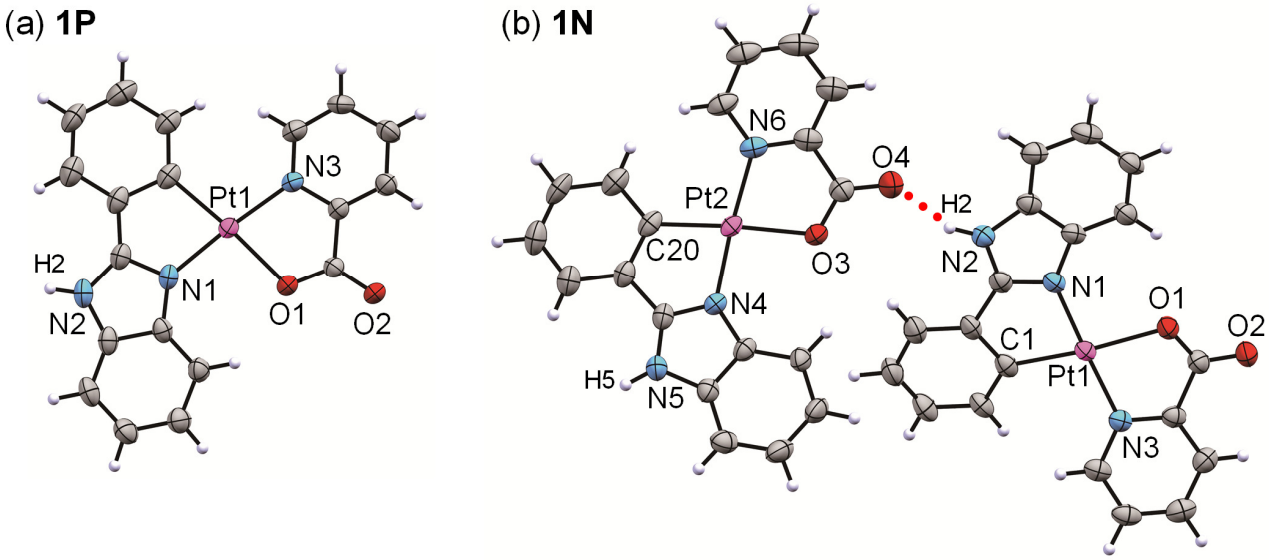

Fig. S1 Asymmetric units of (a) **1P** and (b) **1N**, showing the atom-labelling scheme. Thermal ellipsoids are displayed at the 50% probability level.

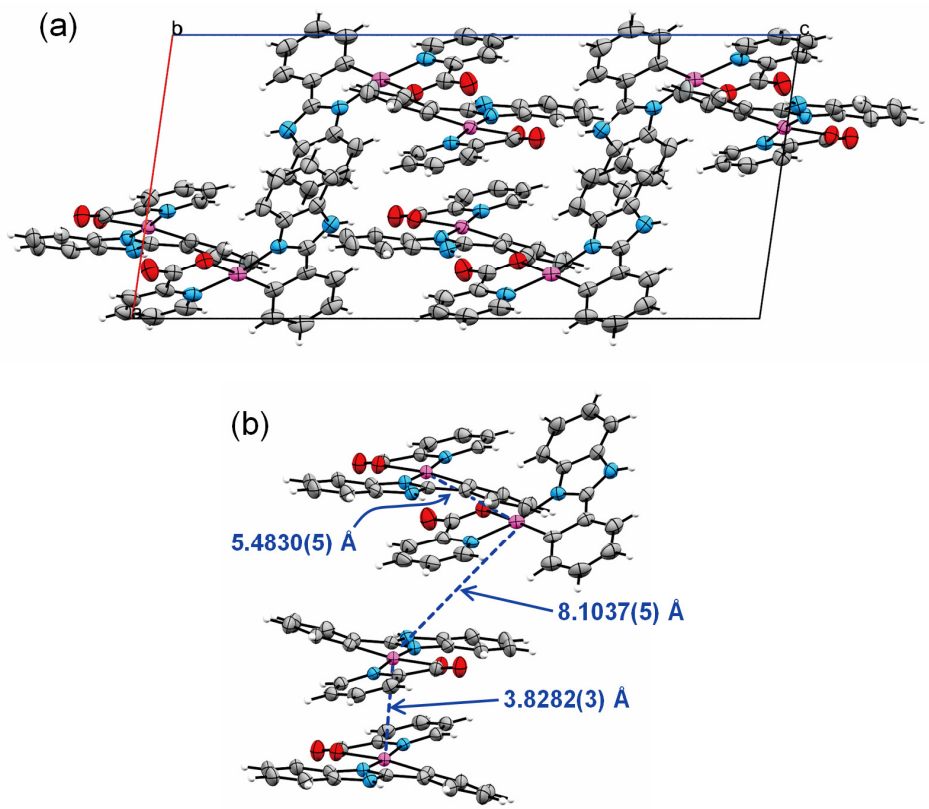

Fig. S2 (a) Packing structure of **1N** viewed along the *b* axis. (b) Three crystallographically independent Pt···Pt distances in **1N**. These Pt···Pt distances are significantly longer than twice the van der Waals radius of Pt (3.5 Å), indicating the negligible Pt···Pt interactions in **1N** in the ground state.

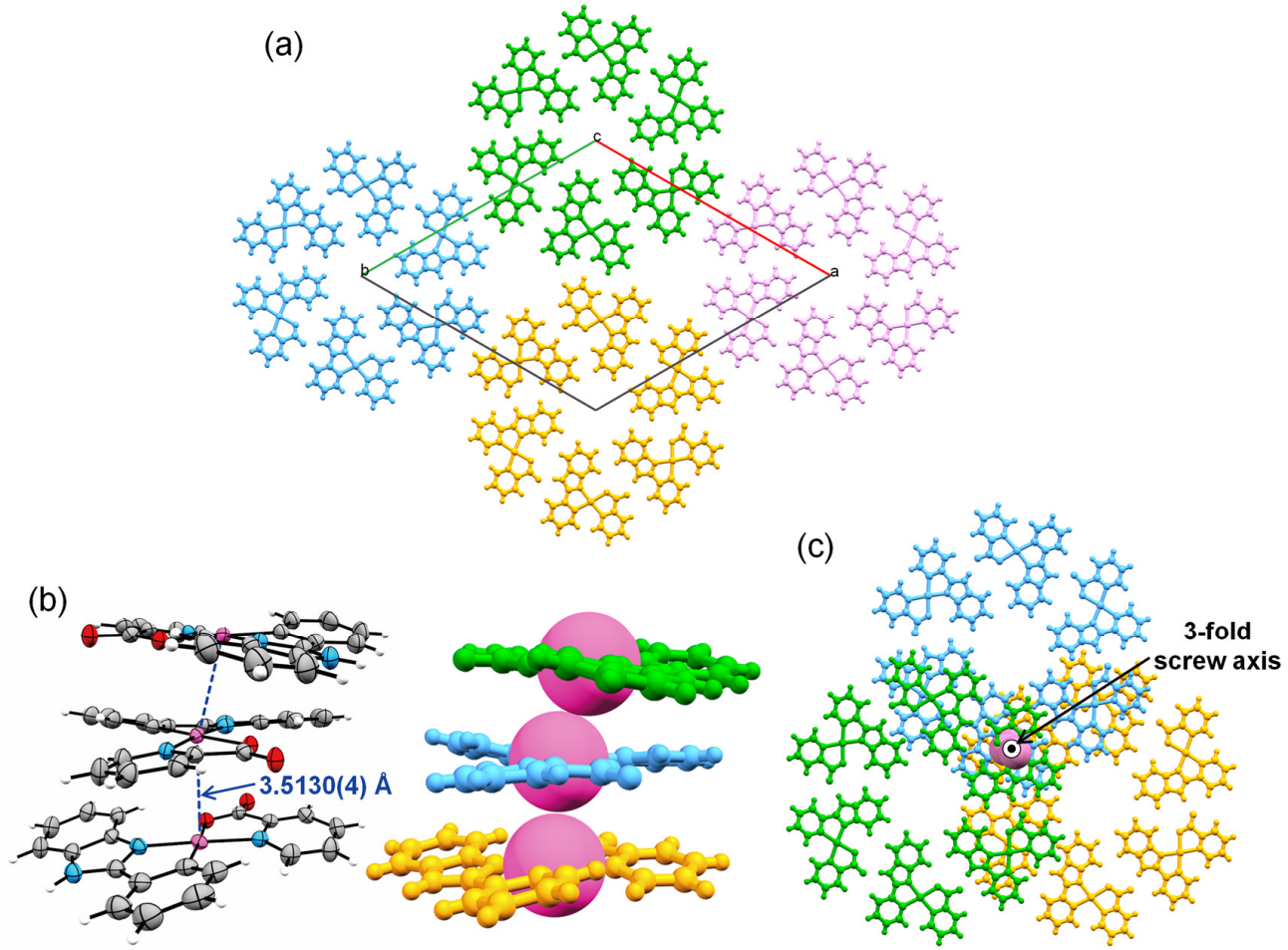

Fig. S3 (a) Two-dimensional sheet structure of **1P**, where each hydrogen-bonded cyclic hexamer is drawn in a different colour for clarity. (b) Pt···Pt interactions of **1P**. In contrast to **1N**, the Pt···Pt distance of **1P** (3.5130(4) Å; see Table S2) is comparable to twice the van der Waals radius of Pt (3.5 Å), indicating the presence of Pt···Pt interactions. (c) Stacking structure of the cyclic hexamer with the Pt···Pt interactions along a 3-fold screw axis.

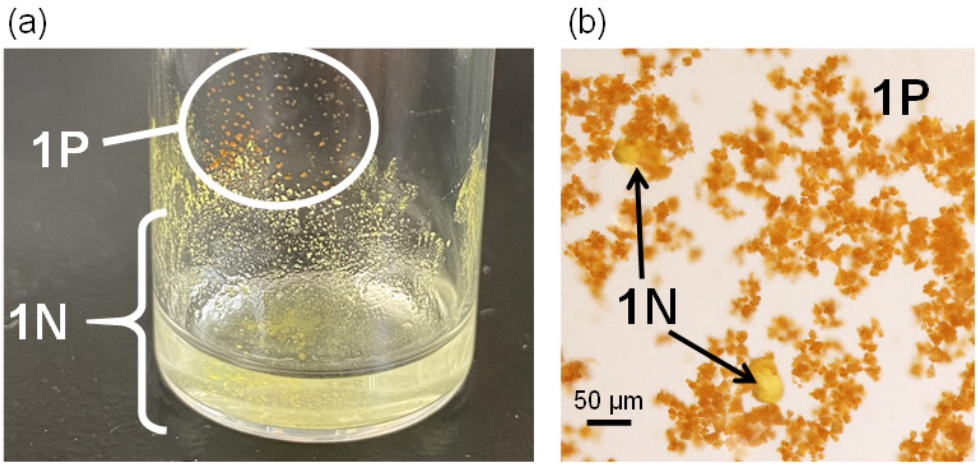

Fig. S4 (a) Photograph of the sample after crystallisation caused by the diffusion of Et_2O vapour into a MeOH solution of **1** (entry 2 in Table S1). Although we have succeeded in obtaining single crystals of **1P** suitable for X-ray crystallography, large amounts of **1N** precipitated with **1P**. (b) Microscopic image of the sample prepared by the slow evaporation of a MeOH solution of **1** (entry 8 in Table S1).

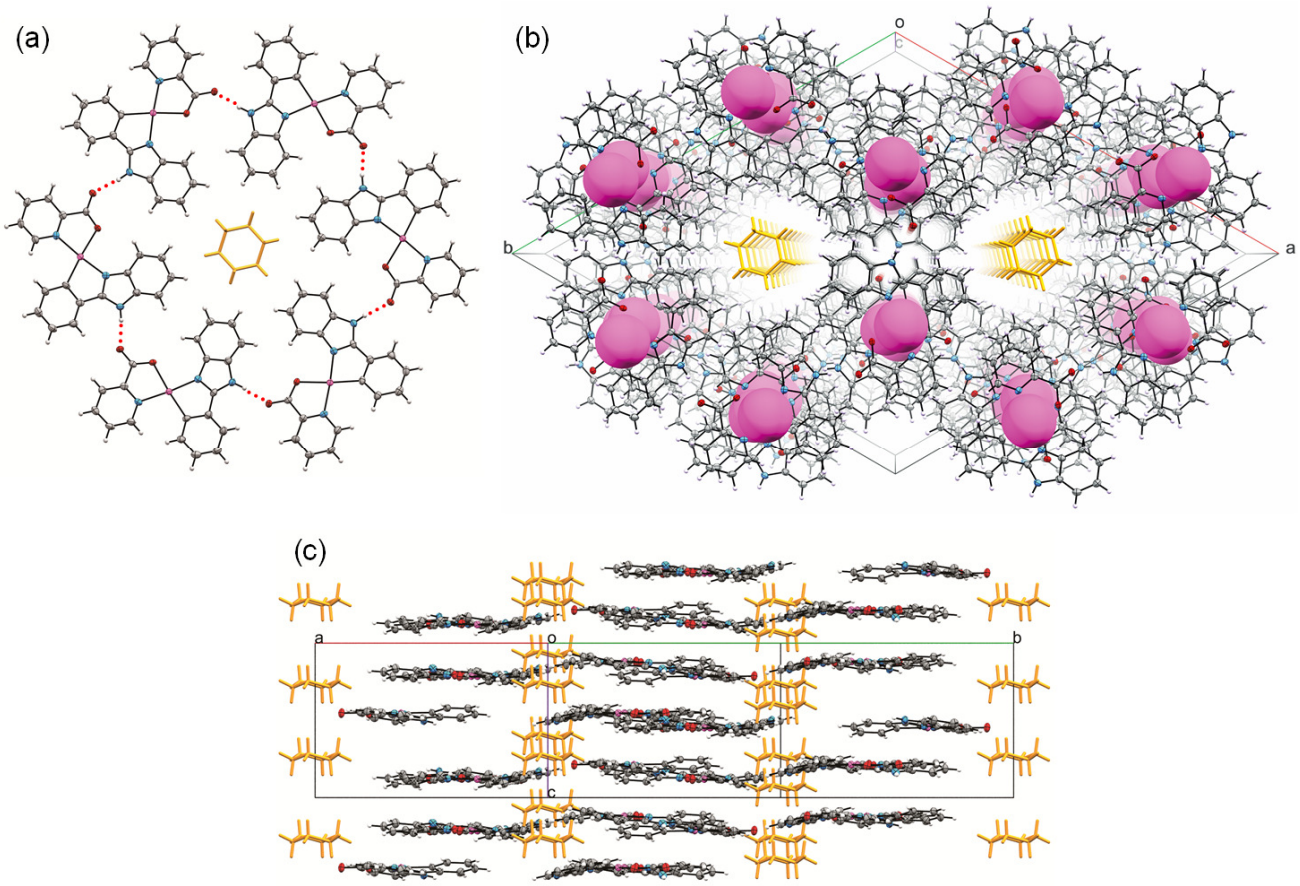

Fig. S5 (a) Hydrogen-bonded hexameric structure of the cyclohexane-included **1P** crystal (**1P**•*c*-Hex). For clarity, only one of the two disordered sites of cyclohexane is plotted. Although the pore diameter and hydrogen-bond lengths of the hexamer are almost identical to those of **1P** (Table S2), a cyclohexane molecule was included in the pore. (b,c) Packing structure of **1P**•*c*-Hex viewed along the *c* axis (b) and from the *bc* plane (c). Pt atoms in (b) are shown as a space-filling model. Cyclohexane molecules (shown in orange) are aligned in the one-dimensional pore.

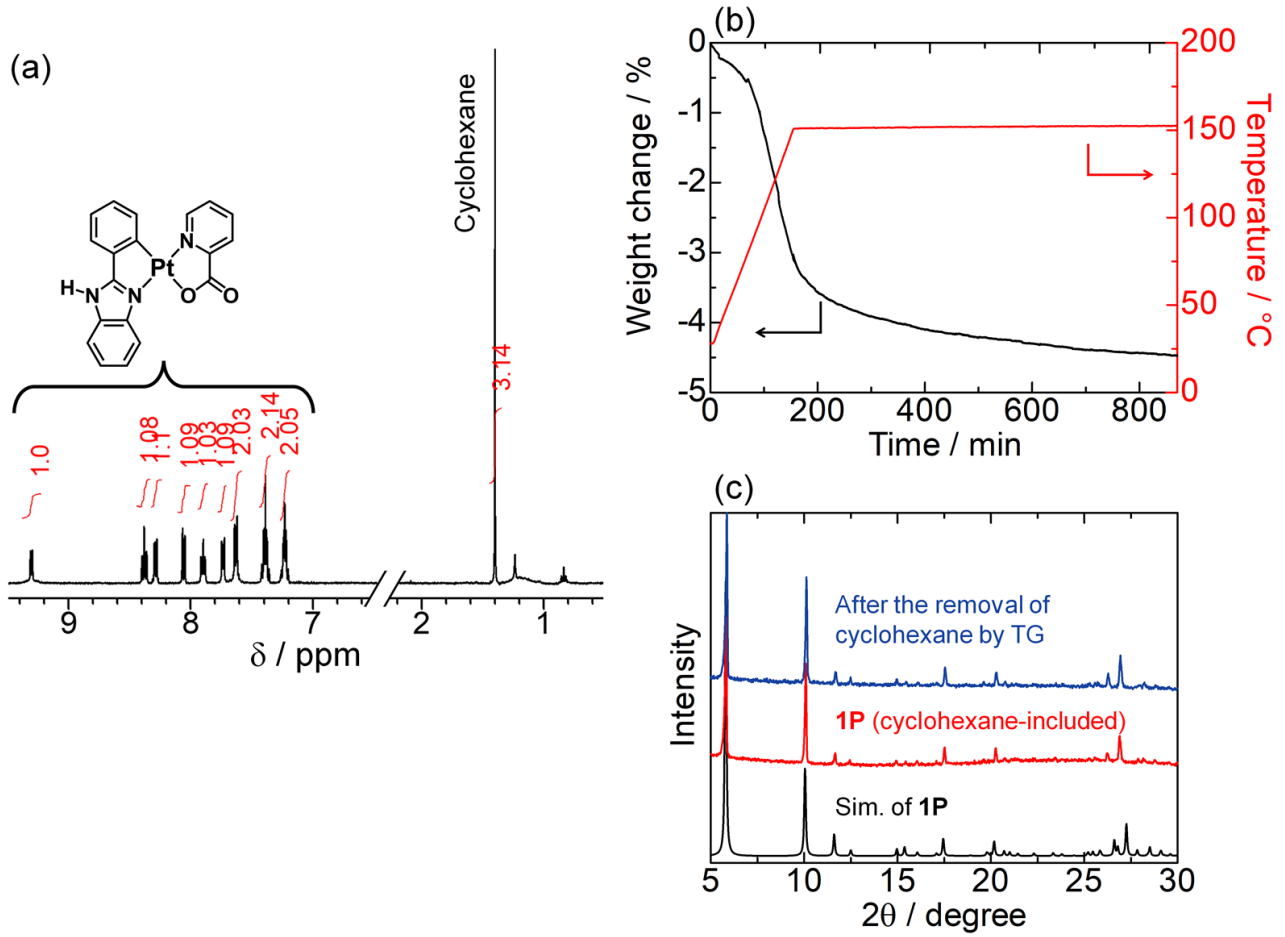

Fig. S6 (a) ^{1}H NMR spectrum of **1P**•*c*-Hex (DMSO-d_6, 400 MHz). (b) Thermogravimetric (TG) analysis of **1P**•*c*-Hex under Ar flow (0.3 L/min), showing the 4.5% weight loss seen at 155 °C. Although the observed integration of the peak due to cyclohexane protons (3.14H) and the observed weight loss (4.5%) are slightly smaller than the theoretical values for the included cyclohexane (4H and 5.2%, respectively), this is likely the result of the gradual desorption of cyclohexane in air before the measurement. (c) PXRD patterns of **1P**•*c*-Hex before (red line) and after (blue line) the removal of cyclohexane in the TG analysis. The porous structure of **1P** was maintained even after the desorption of cyclohexane (i.e. permanent porosity).

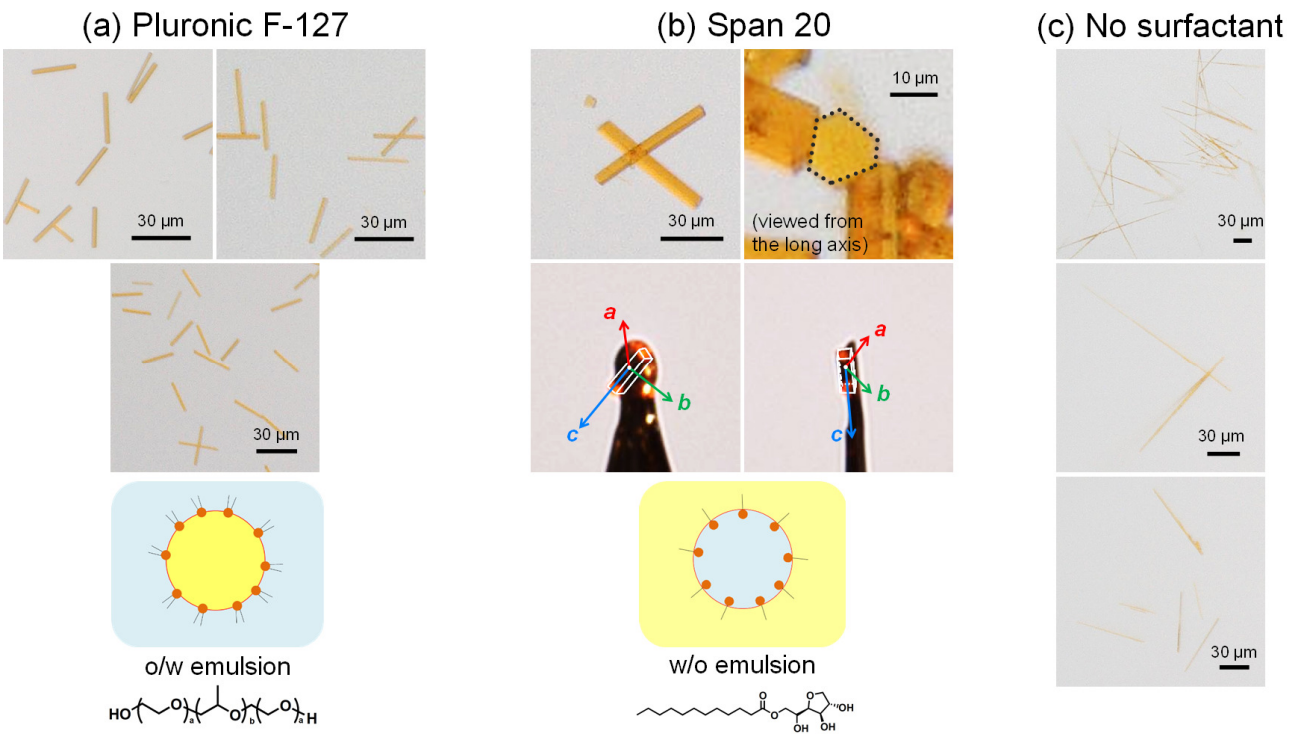

Fig. S7 Photographs of **1P** crystals prepared by using a cyclohexane emulsion in the presence of (a) Pluronic F-127 or (b) Span 20, or (c) in the absence of surfactants. Needle-like crystals of **1P** were obtained regardless of whether the surfactant was Pluronic F-127 (stabilising the o/w emulsion) or Span 20 (stabilising the w/o emulsion). Although **1P** was also formed in the absence of surfactant, the crystals were much thinner. Since the long axis direction of the crystal **1P** corresponds to the *c* axis, it is likely that the presence of surfactants at the liquid-liquid interface controls the growth rate of the crystals of **1P**.

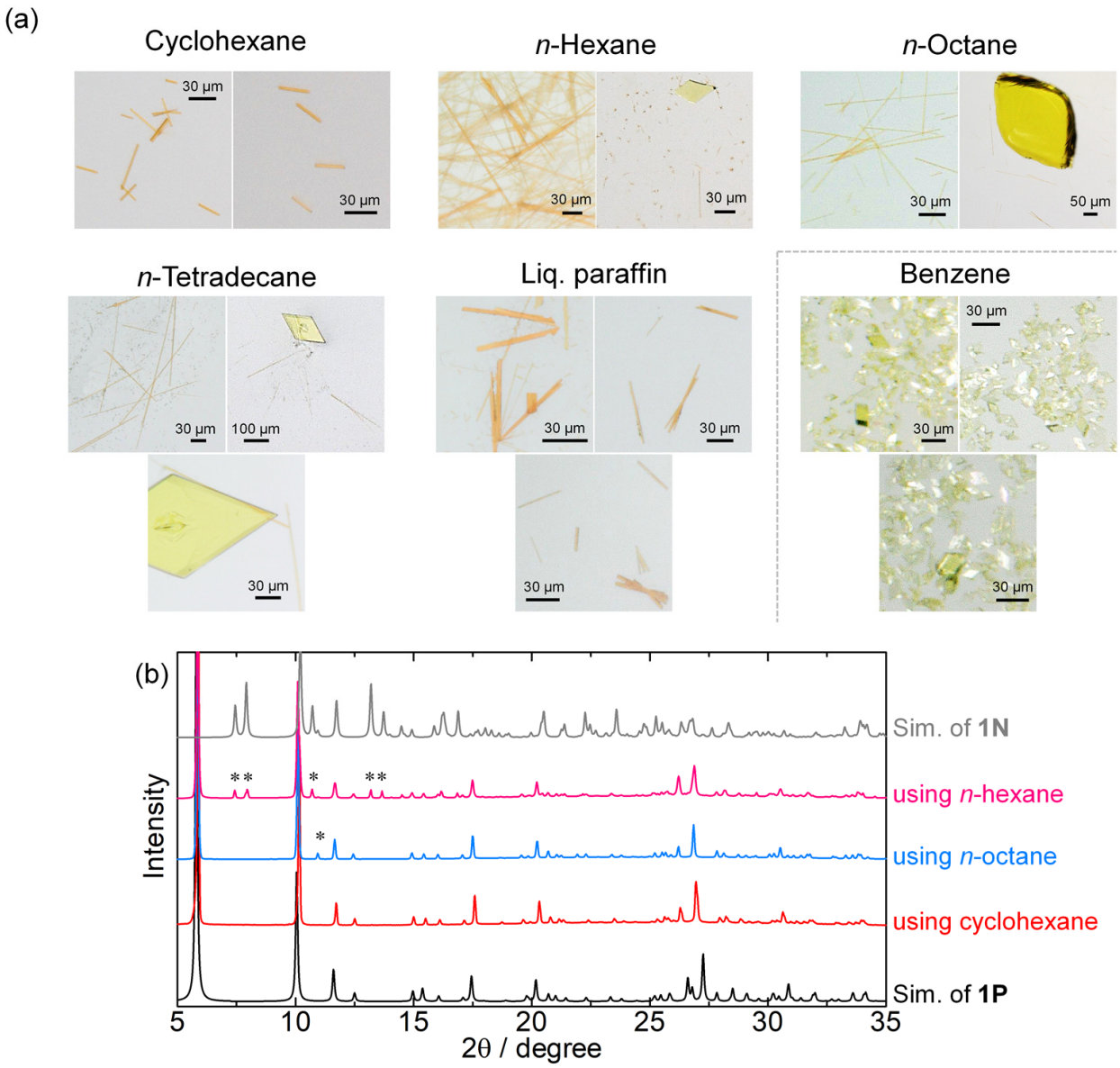

Fig. S8 (a) Photographs of crystals obtained using emulsions of cyclohexane, *n*-hexane, *n*-octane, *n*-tetradecane, liquid paraffin, and benzene in the presence of Pluronic F-127. When *n*-hexane, *n*-octane, and *n*-tetradecane were used, small amounts of **1N** contaminated the **1P**. Although the molecular size, shape (symmetry), and Lennard-Jones collision diameter of benzene are similar to those of cyclohexane, the emulsion of benzene only afforded **1N**, probably due to the presence of the π-system in benzene. (b) PXRD patterns of crystalline powders of **1P** prepared using emulsions of cyclohexane (red line), *n*-hexane (pink line), and *n*-octane (blue line). The black and grey lines indicate the simulated patterns based on the crystal structures of **1P** and **1N**, respectively. When *n*-hexane and *n*-octane were used, small peaks assignable to **1N** appeared (as indicated by asterisks). When *n*-tetradecane or liquid paraffin was used, PXRD measurement was difficult because of the low yield (*n*-tetradecane) or difficulty in collection resulting from the high viscosity (for liquid paraffin). Therefore, the products were identified by single crystal X-ray diffraction analysis (see Table S4).

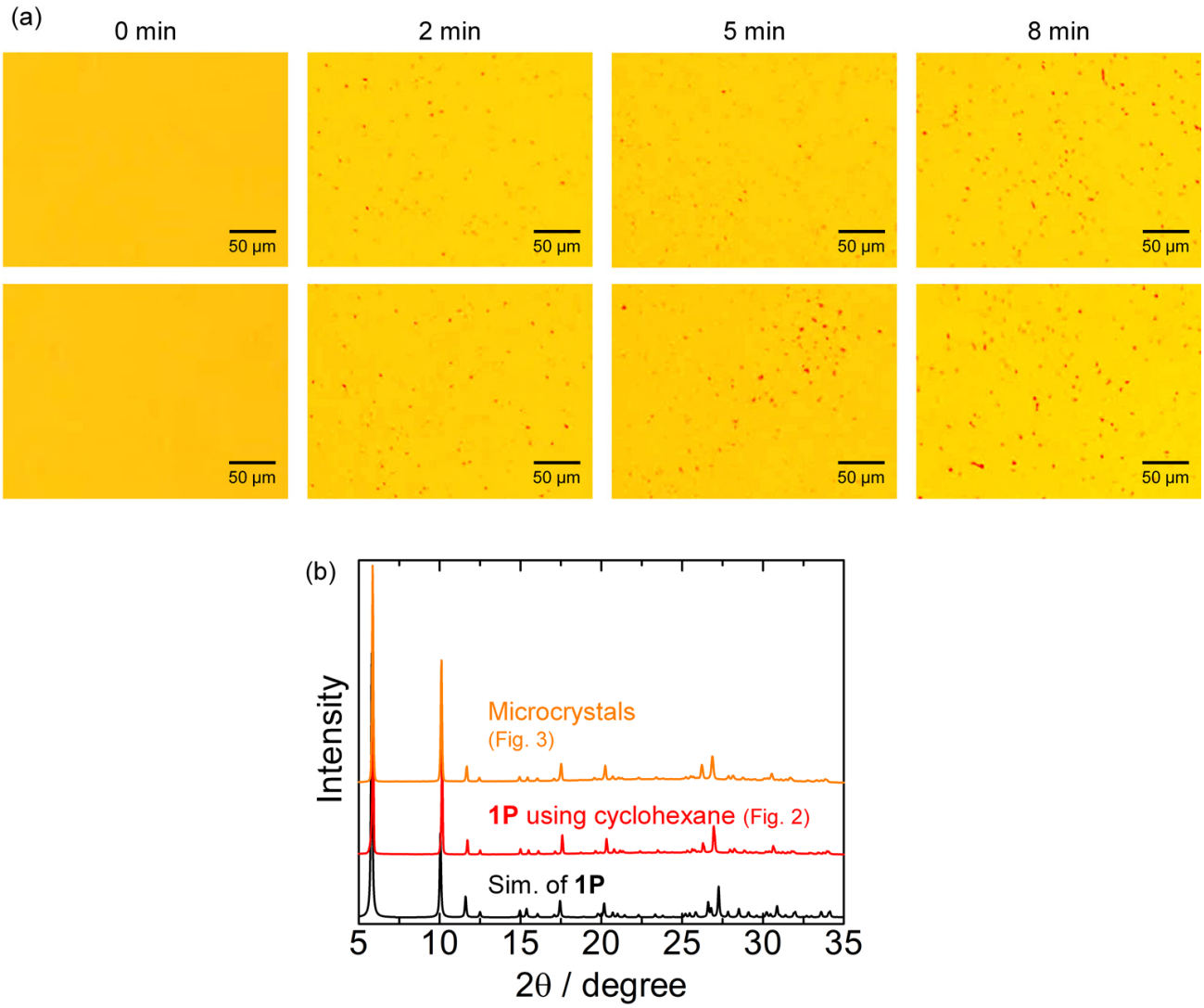

Fig. S9 (a) Optical microscopic images of the interface between a solution of **1** in MeOH/H_2O (v/v = 1/1) mixture and liquid paraffin. (b) PXRD patterns of microcrystals obtained by layering of a solution of **1** onto liquid paraffin (orange line), or **1P** prepared using cyclohexane emulsion (red line). The black line indicates the simulated pattern based on the crystal structure of **1P**.

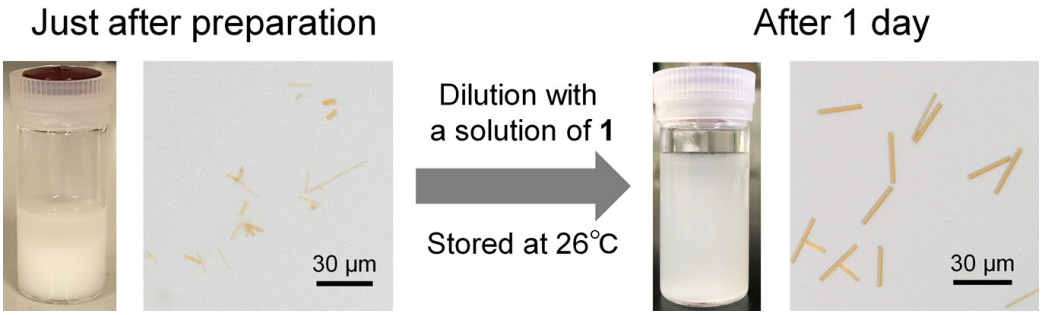

Fig. S10 Photographs of the **1P** crystals just after preparation of cyclohexane-MeOH/H_2O emulsion (left) and after 1 day (right).

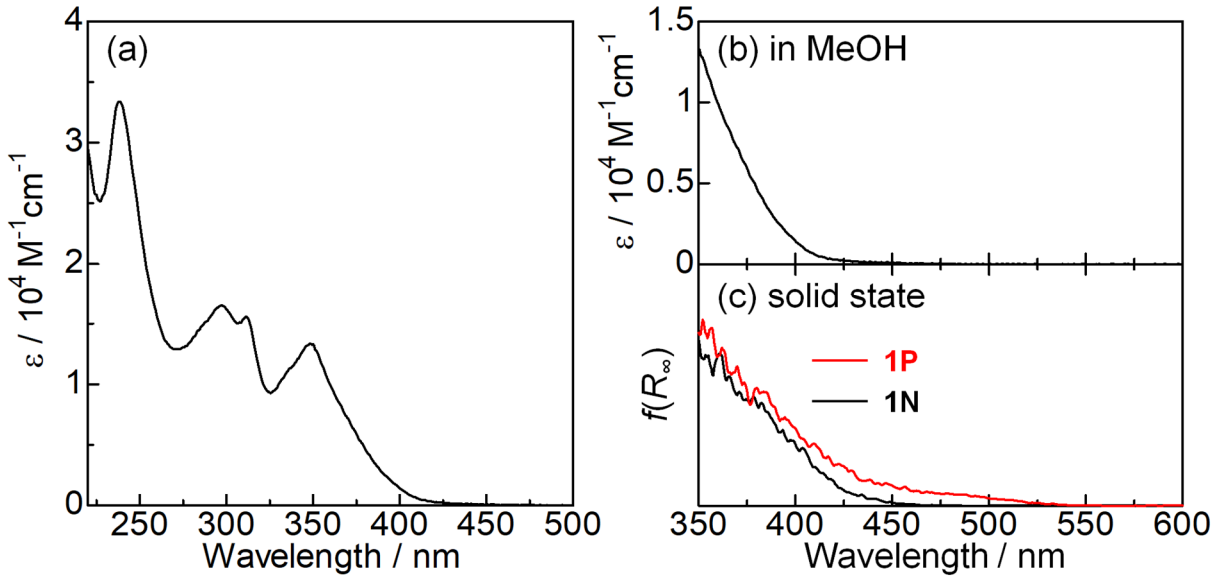

Fig. S11 (a) UV-vis absorption spectrum of **1** in methanol at 298 K, and (b) the magnification of the 350-600 nm region. Intense absorption bands below 330 nm corresponded to the singlet ligand-centred $^1\pi\pi^*$ transition band of the pbim ligand.[S12] In addition, the moderately intense absorption band at approximately 330-450 nm (λ_{max} = 348 nm, ε_{348} = 1.3 × 10^4 $M^{-1}cm^{-1}$) is mainly attributed to the singlet metal-to-ligand charge transfer (^{1}MLCT) excitation. (c) UV-vis diffuse-reflectance spectra of **1P** (red line) and **1N** (black line) in the solid state. The absorption edge of **1N** is almost similar to that of **1** in solution, which is consistent with the absence of Pt···Pt interactions in **1N**. On the other hand, **1P** displayed a new broad absorption band at 450-500 nm, which is assignable to the ^{1}MMLCT transition originating from the Pt···Pt interactions.

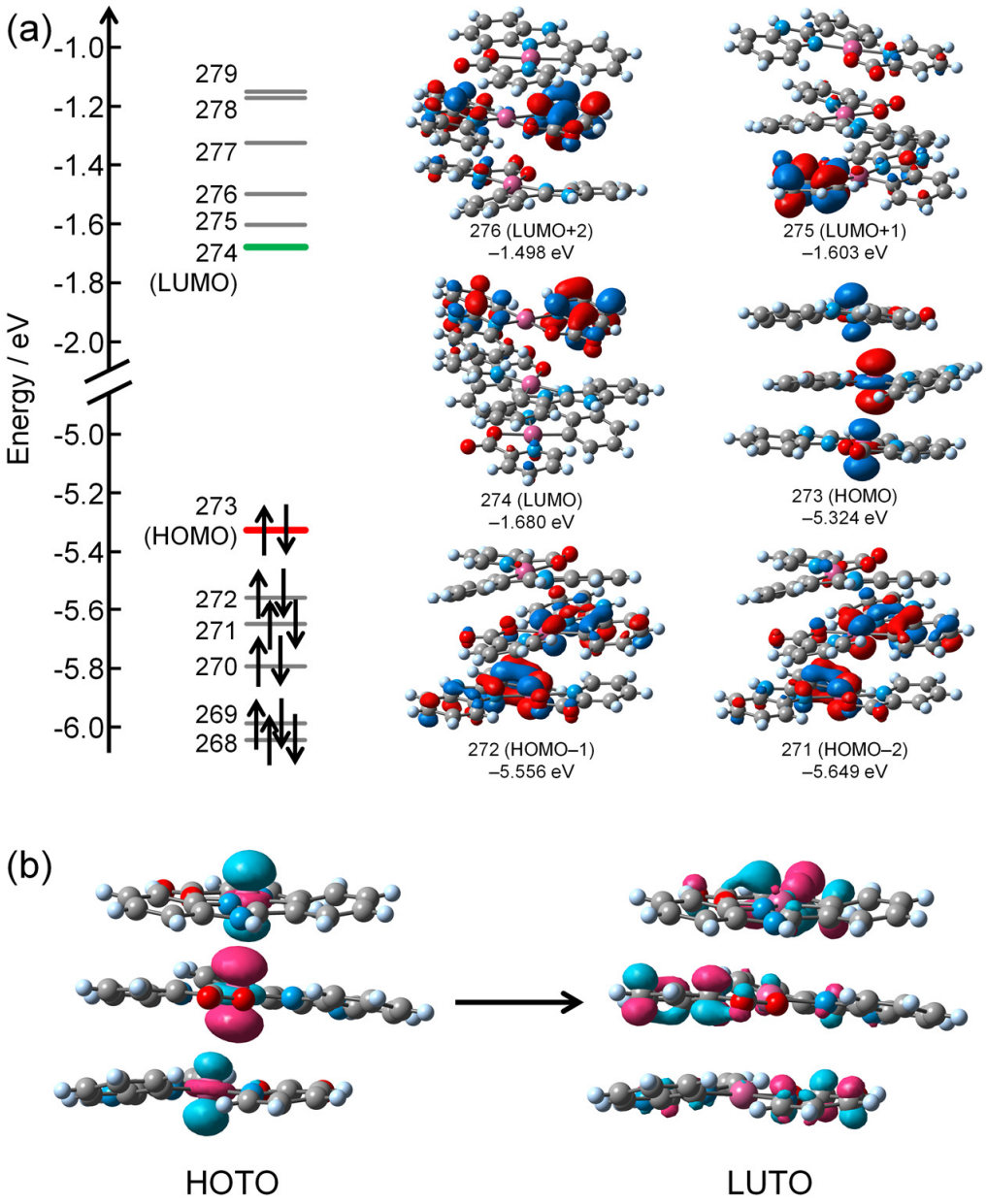

Fig. S12 (a) Kohn-Sham orbitals at the frontier region of the trimeric unit of **1P** (isovalue = 0.035). HOMO is assignable to the dσ* orbital between three Pt atoms, while LUMO to LUMO+2 are delocalised on the π* orbitals of the pic ligand as well as the pbim ligand. (b) Natural transition orbitals (NTOs) of the trimeric unit of **1P** for the 1st vertical excitation (λ = 442.60 nm, f = 0.0443). The highest occupied transition orbital (HOTO) and the lowest unoccupied transition orbital (LUTO) indicate the occupied "hole" and the unoccupied "electron", respectively. This result suggests that the lowest excited state of **1P** could be assignable to the dσ*→π* transition, i.e., MMLCT transition.

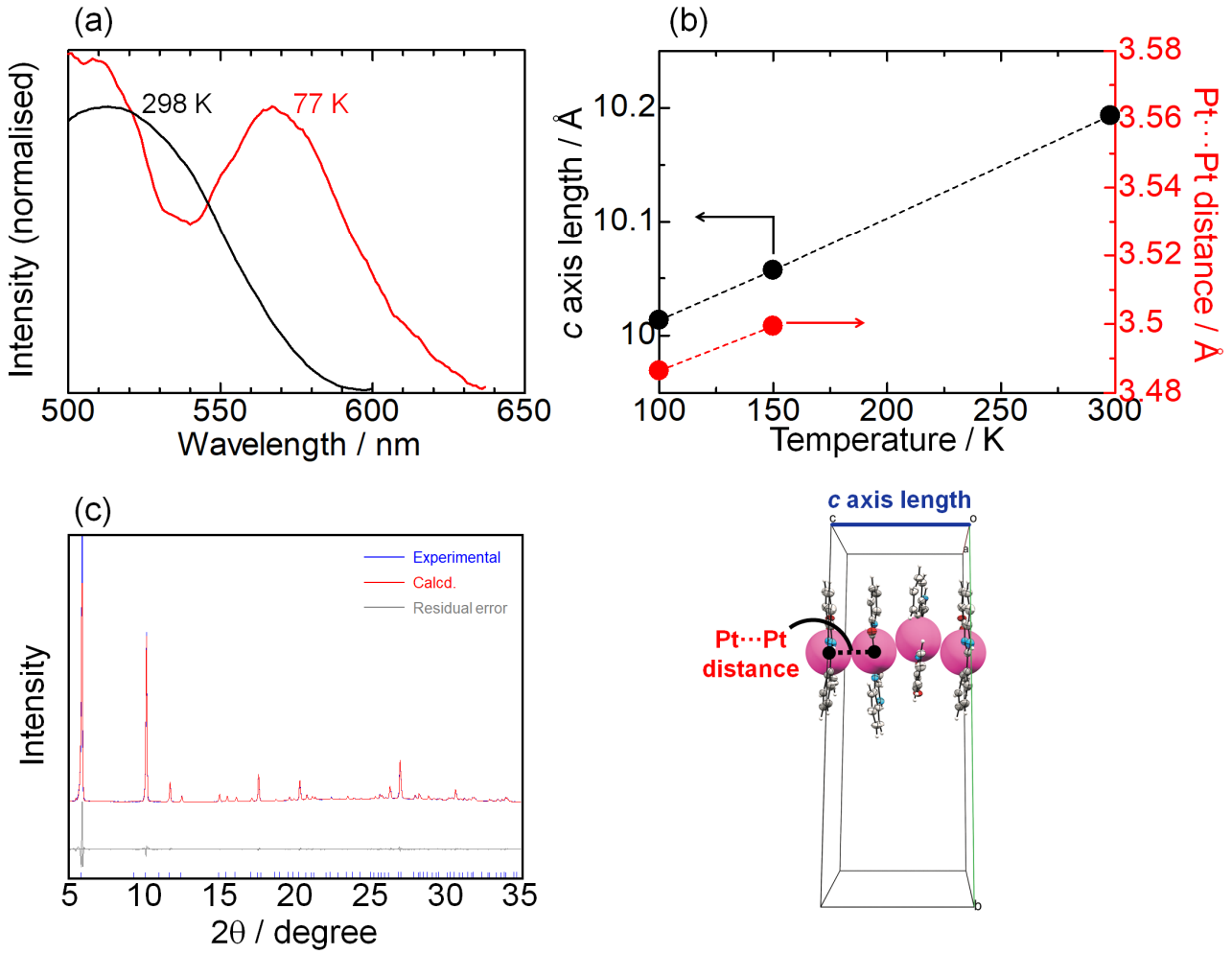

Fig. S13 (a) Excitation spectra of **1P** (λ_{em} = 690 nm (298 K) or 720 nm (77 K)) in the solid state at 298 K (black lines) and 77 K (red lines). As observed in emission spectra (Fig. 4), excitation bands also showed a significant red-shift at 77 K, due to the shortening of Pt···Pt distances.[S13] (b) The temperature dependences of *c* axis lengths (black) and Pt···Pt distances (red) of **1P**. The data at 100 K and 150 K were obtained by SXRD analysis (Tables S2 and S7), while the lattice constant at 298 K was obtained by the refinement of the lattice constants for the experimental PXRD pattern (Fig. S13(c)). Both the *c* axis lengths (Pt···Pt stacking direction) and the Pt···Pt distances shortened with a temperature decrease, consistent with the red-shift of the emission band of **1P** at low temperature. (c) Experimental PXRD pattern of **1P** (blue line, taken from the data given in Fig. 2), and calculated (red line) and difference (grey line) between the experimental and calculated PXRD patterns. Short blue vertical bars below the difference pattern indicate the positions of allowed Bragg reflections. Lattice constants were refined by the whole powder pattern decomposition (WPPD) method by using *TOPAS 4* program[S14] as follows: a = 30.385(2) Å, c = 10.1932(7) Å, V = 8150(1) Å^3, R_{wp} = 6.158%.

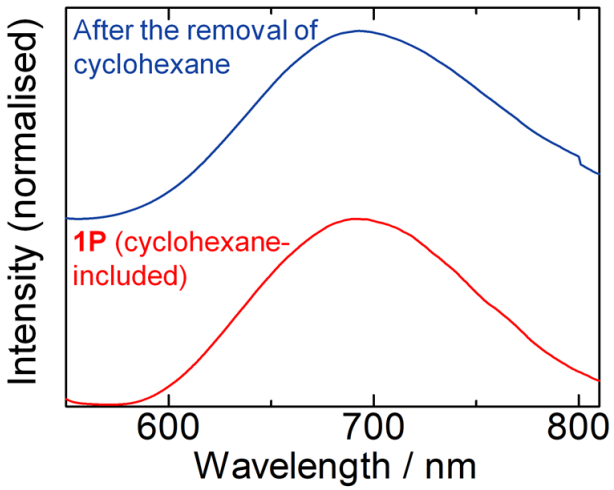

Fig. S14 Emission spectra (λ_{ex} = 500 nm) of **1P**•*c*-Hex before (red line) and after (blue line) the removal of cyclohexane at 155 °C in the thermogravimetric analysis (see Fig. S6). Consistent with the permanent porosity, the luminescence of **1P** was maintained even after the removal of cyclohexane (λ_{max} = 692 nm → 693 nm).

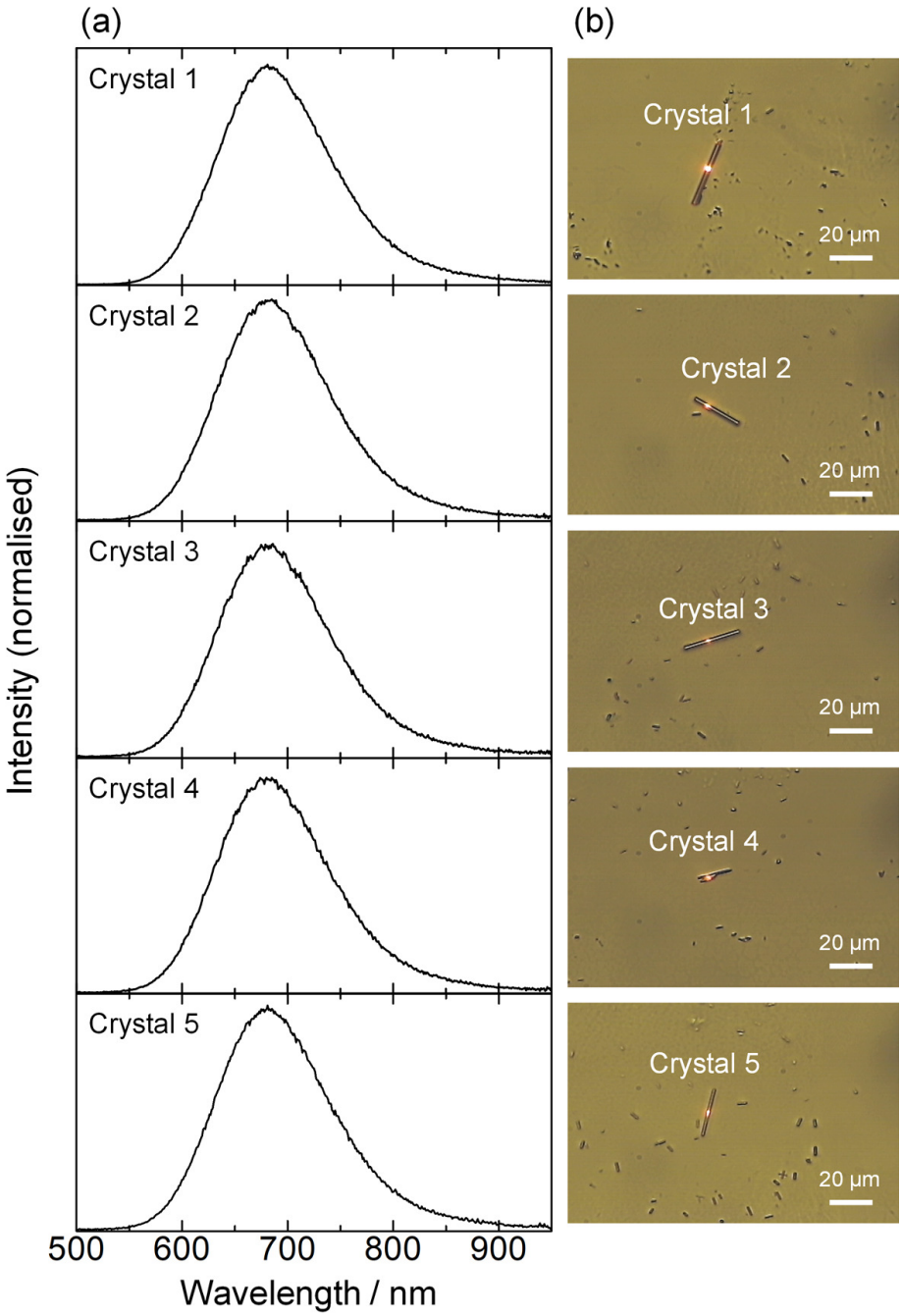

Fig. S15 (a) Emission spectra (λ_{ex} = 488 nm) and (b) corresponding optical microscopic images of single crystals of **1P** formed in situ with the use of a cyclohexane emulsion. All of the crystals 1-5 exhibited identical broad emission spectra with emission maximum at λ_{max} = 680 nm. These emission spectra are almost identical to that of bulk sample of **1P** (Fig. 4), indicating the high purity of bulk sample **1P** prepared with the use of the cyclohexane emulsion.

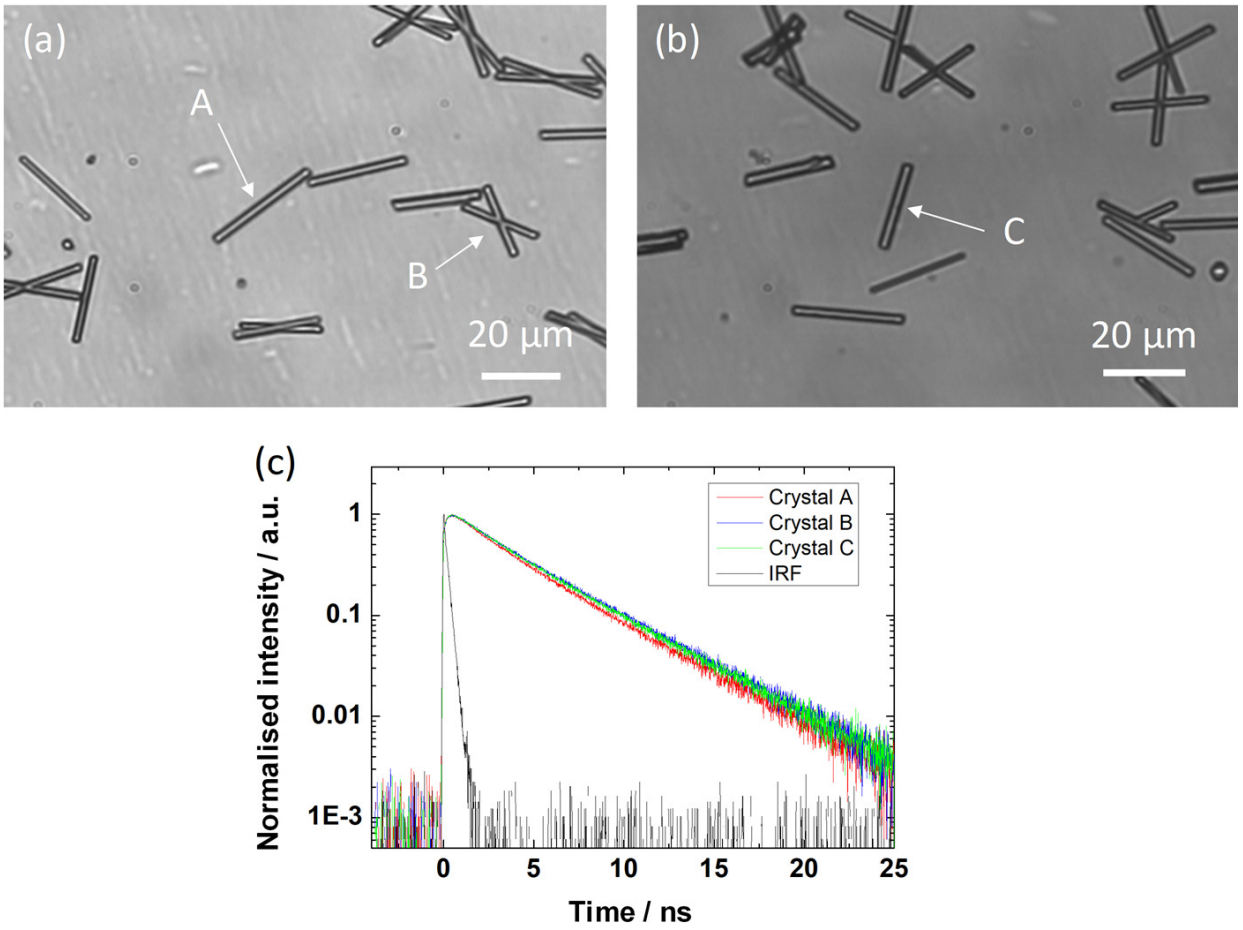

Fig. S16 (a,b) Optical microscopic images and (c) emission decay curves (λ_{ex} = 488 nm) for single crystals of **1P** formed in situ with the use of a cyclohexane emulsion. The black line in (c) shows the instrument response function (IRF). All of the crystals A-C exhibited nearly identical emission decay profiles with averaged emission lifetimes τ_1 = 3.3 ± 0.4 ns (A_1 = 0.77) and τ_2 = 6.7 ± 1.4 ns (A_2 = 0.22). Although the emission lifetime of **1P** was significantly shorter than those of typical ^{3}MMLCT phosphorescent Pt(II) complexes (~10^2 ns), the weak emission intensity of **1P** (emission quantum yield was below the detection limit, i.e. Φ < 0.01) suggests the presence of rapid nonradiative decay processes in **1P**.

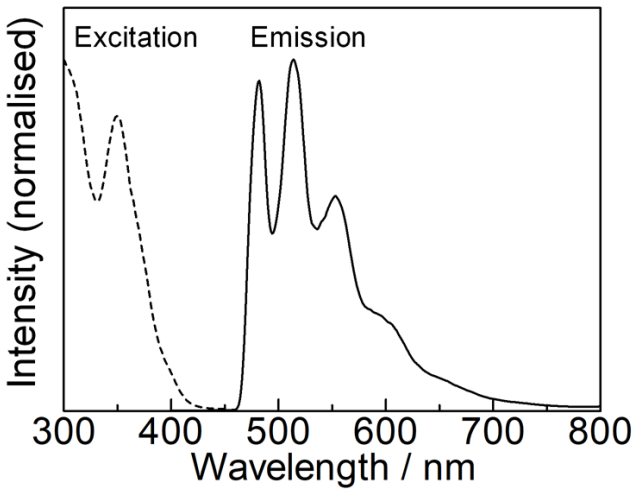

Fig. S17 Emission (solid line; λ_{ex} = 400 nm) and excitation (dashed line; λ_{em} = 481 nm) spectra of **1** in a MeOH/EtOH [1:1 (v/v)] glass at 77 K. A vibronically structured emission band (λ_{max} = 482, 514, and 553 nm) is assignable to the $^3\pi\pi^*$ emission centred at the pbim ligand, similar to those of previously reported Pt(II) complexes bearing the *N*-substituted pbim ligand.[S15]

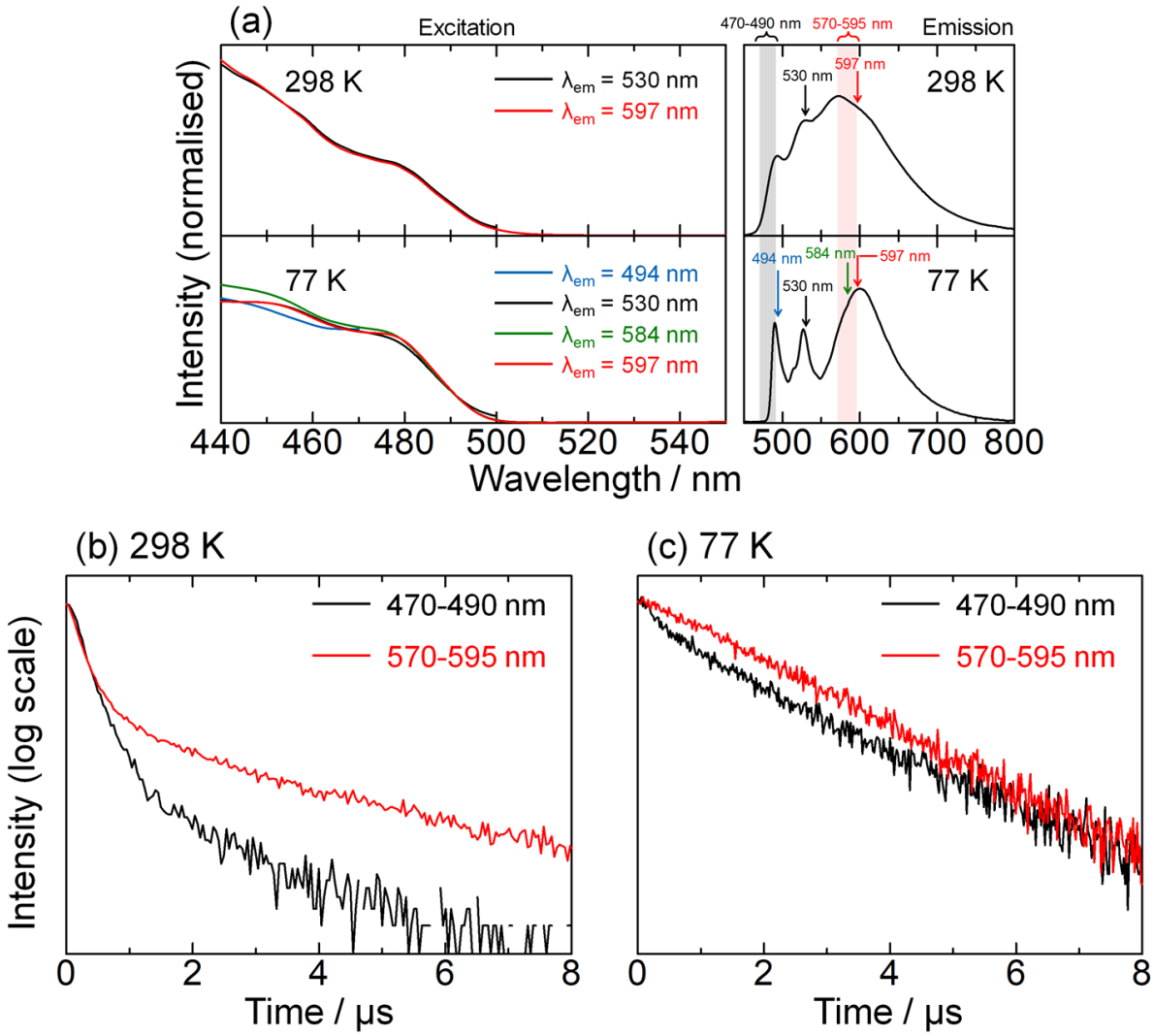

Fig. S18 (a) Excitation spectra of **1N** detected at different emission wavelengths at 298 K and 77 K, and the corresponding emission spectra (λ_{ex} = 350 nm). Regardless of whether it was detected in the high energy $^3\pi\pi^*$ emission band (λ_{em} = 494 and 530 nm) or the low energy emission band (λ_{em} = 584 and 597 nm), no significant change was observed in the excitation spectra. (b,c) Emission decay curves of **1N** at (b) 298 K and (c) 77 K detected at 470-490 nm (black) and 570-595 nm (red). The emission decay curves largely depended on the detection wavelength region. Particularly, at 77 K, emission decay in the 470-490 nm region was analysed with two exponentials, whereas only one decay component was observed in the 570-595 nm region. These excitation spectra and emission decay curves imply the occurrence of excimer formation from a monomeric $^3\pi\pi^*$ excited state (or energy transfer from $^3\pi\pi^*$ excited state to a dimer state in some structural defects). The detailed photophysical data are summarised in Table S6.

Table S1 Results on the crystallisation by using typical methods (after 1 week). Because **1** is sufficiently soluble only in high polarity solvents, only methanol and DMF were available as good solvents for crystallisation.

Entry	Good Solv.	Poor Solv.	Concentration	Temp.	Product
1	MeOH/H_2O	–	0.125 mM	4 °C	**1N** (for SXRD; Fig. 1(a))
2	MeOH	Et_2O	Saturated	10 °C	**1P** (for SXRD; Fig. 1(b)) + **1N**
3	MeOH	Et_2O	Saturated	25 °C	**1N**
4	MeOH	Et_2O	Half of entry 2	10 °C	**1P** + **1N**
5	MeOH	CH_2Cl_2	Saturated	10 °C	**1N**
6	MeOH	CH_2Cl_2	Saturated	25 °C	**1N**
7	MeOH+LiOMe	AcOH	Saturated	25 °C	**1P** + **1N**
8	MeOH (slow evaporation)	–	Saturated	15 °C	**1P** + **1N**
9	DMF	Et_2O	Saturated	10 °C	**1P** + **1N**
10	DMF	acetone	Saturated	10 °C	**1N**
11	DMF	acetone	Saturated	25 °C	**1N**
12	DMF	MeCN	Saturated	10 °C	**1N**
13	DMF	MeCN	Saturated	25 °C	**1N**
14	DMF	AcOH	Saturated	25 °C	**1N**
15	DMF+LiOMe	AcOH	Saturated	25 °C	**1N**

Table S2 Selected interatomic distances and angles, and pore diameters of **1N**, **1P**, and solvent-included **1P** (**1P**•solv).

	1P•*c*-Hex (150 K)	**1P**•*c*-Hex (100 K)	**1P**•Paraffin (150 K)	**1P** (150 K)	**1N** [a] (150 K)	
			Distances / Å			
Pt1···Pt1	3.4994(4)	3.4864(4)	3.4978(8)	3.5130(4)	–	
Pt1-N1	1.999(3)	1.999(3)	1.984(9)	1.997(3)	2.006(4),	2.001(4)
Pt1-C1	2.021(3)	2.025(4)	2.03(1)	2.017(4)	1.998(4),	2.012(5)
Pt1-N3	2.028(3)	2.039(3)	2.06(1)	2.028(3)	2.021(4),	2.017(4)
Pt1-O1	2.105(2)	2.107(2)	2.096(8)	2.111(2)	2.117(3),	2.112(3)
N2···O2	2.713(6)	2.718(5)	2.72(2)	2.718(7)	2.667(5), (N2···O4)	2.705(5) (N5···O2)
			Angles / degree			
Pt1···Pt1···Pt1	151.23(2)	151.03(2)	150.85(2)	149.52(2)	–	
N1-Pt1-O1	95.4(1)	95.6(1)	96.6(4)	95.8(1)	97.7(1),	96.5(1)
N1-Pt1-N3	174.4(1)	174.4(1)	175.5(4)	174.8(1)	174.7(1),	170.4(1)
N1-Pt1-C1	80.1(1)	80.0(2)	79.1(6)	80.0(2)	79.9(2),	80.3(2)
N3-Pt1-O1	79.8(1)	79.8(1)	79.6(4)	80.1(1)	79.9(1),	80.0(1)
C1-Pt1-O1	175.5(1)	175.5(1)	175.8(5)	175.8(1)	172.9(2),	172.4(2)
C1-Pt1-N3	104.7(1)	104.7(1)	104.6(5)	104.0(1)	103.0(2),	104.2(2)
N2-H2···O2	173.5	173.1	174.6	175.3	158.1 (N2-H2···O4)	175.6 (N5-H5···O2)
			Pore diameters / Å			
H-H distance (*l*)[b]	8.10	8.07	8.22	8.31	–	
Pore diameter (*d*)[b]	7.04	7.01	7.16	7.25	–	

[a] There are two crystallographically independent molecules of **1** in the crystal. Pt2, C20, N4, N5, N6, O3, and O4 corresponded to Pt1, C1, N1, N2, N3, O1, and O2, respectively.

[b] The definition of the H-H distance (*l*) and pore diameter (*d*) are shown in the right figure.

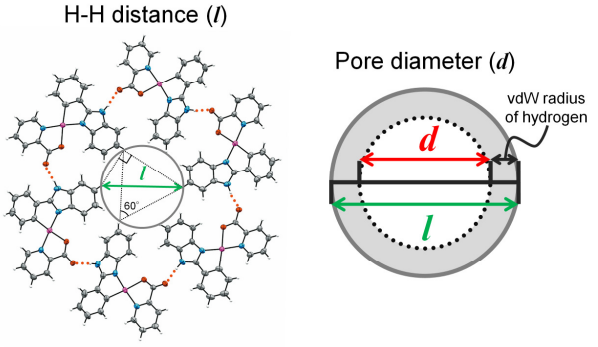

Table S3 Crystal parameters of **1N** obtained by three crystallisation methods. The details of refinement data for entry 1 are summarised in Table S7. For entries 2 and 3, only lattice constants were determined. The cyclohexane-containing solution was prepared by using the separating funnel.

Entry	1	2	3
Crystallisation method	From a solution of **1** (0.125 mM) in MeOH/H_2O at 4 °C	Seed crystal of **1P** was added to a solution of **1** (0.25 mM) in MeOH/H_2O at 25 °C and slowly evaporated	From a solution of **1** (0.125 mM) in a MeOH/H_2O (containing 0.35 mM cyclohexane) at 4 °C[a]
Temperature (K)	150	150	150
Crystal system	Monoclinic	Monoclinic	Monoclinic
Space group	$P2_1/c$ (#14)	$P2_1/c$ (#14)	$P2_1/c$ (#14)
a (Å)	11.0034(1)	10.9929(2)	11.0084(1)
b (Å)	12.6502(1)	12.6063(2)	12.5864(1)
c (Å)	23.9841(2)	23.9971(3)	24.0033(2)
β (deg)	98.435(1)	98.103(1)	98.024(1)
V (Å^3)	3302.36(5)	3292.31(9)	3293.24(5)

a No crystals were obtained at 25 °C.

Table S4 Crystal parameters of **1P** obtained by several crystallisation methods. The details of refinement data for entries 1, 2, and 4 are summarised in Table S7. For entry 3, only lattice constants were determined. The lattice constants slightly affected by the kind of solvents, suggesting the inclusion of solvent molecules in the pore.

Entry	1	2 (**1P**•*c*-Hex)	3 (**1P**•Tetradecane)	4 (**1P**•Paraffin)
Crystallisation method	Vapour diffusion (MeOH/Et_2O)	Emulsion of cyclohexane	Emulsion of tetradecane	Emulsion of liquid paraffin
Temperature (K)	150	150	150	150
Crystal system	Trigonal	Trigonal	Trigonal	Trigonal
Space group	$R\bar{3}$ (#148)	$R\bar{3}$ (#148)	$R\bar{3}$ (#148)	$R\bar{3}$ (#148)
a, b (Å)	30.4714(3)	30.2896(3)	30.2444(6)	30.402(2)
c (Å)	10.0419(1)	10.0570(1)	10.0562(2)	10.0404(8)
V (Å^3)	8074.8(2)	7990.7(2)	7966.3(4)	8037(1)

Table S5 Results from the crystallisations from MeOH/H_2O-alkane emulsion ([**1**] = 0.125 mM, [Pluronic F-127] = 0.1 mM). The product selectivity was not directly related to the density, viscosity, or relative permittivity of the organic solvent. For *n*-hexane, *n*-octane, and *n*-tetradecane, the decreased selectivity could be due to their less symmetries and less-desirable sizes, relative to cyclohexane (as discussed in the main text). For liquid paraffin, the high selectivity could originate from the stabilisation of the emulsion due to the very high viscosity of liquid paraffin.

	Density (g/mL)	Viscosity (mPa·s)	Relative permittivity	Temperature (°C)	Product
cyclohexane	0.774-0.782	1.02	2.024	10	**1P**
n-hexane	0.66	0.294	1.880	10	**1P** + **1N**
n-octane	0.698-0.704	0.547	1.948	10	**1P** + **1N**
n-tetradecane	0.760-0.766	2.13	2.06 [a]	10	**1P** + **1N** [c]
liq. paraffin (Wako Pure Chem. Co.)	0.86-0.89	67 [b]	2.1-2.5	10	**1P** [d]
MeOH	0.792	0.59	32.66	–	–
H_2O	0.997	0.890	80.4	–	–

[a] Ref. S16. [b] Ref. S17. [c] Only small amount of crystals were obtained. [d] Because of the high viscosity of liquid paraffin, it was very difficult to collect the crystals formed. Instead, the crystals obtained at the MeOH/H_2O-liquid paraffin interface were characterised with the PXRD measurement (Fig. S9(b)) after the microscopic observation of the MeOH/H_2O-liquid paraffin interface (Fig. 3).

Table S6 Photophysical data of **1N** and **1P**. Because **1N** exhibited the dual emission from both monomeric and excimeric excited states, it is unable to determine the radiative and nonradiative rate constants (k_r and k_{nr}, respectively).

	T / K	λ_{max}[a]	Φ[b]	Lifetime	
				λ[c] / nm	τ[d] (A[e])
1N	298	493, 530, 573	0.10	470-490	τ_1 = 0.25 μs (A_1 = 0.978) τ_2 = 1.18 μs (A_2 = 0.022)
				570-595	τ_1 = 0.22 μs (A_1 = 0.922) τ_2 = 1.69 μs (A_2 = 0.078)
	77	490, 526, 600	0.38	470-490	τ_1 = 0.46 μs (A_1 = 0.627) τ_2 = 2.13 μs (A_2 = 0.174)
				570-595	τ = 1.95 μs
1P	298	692	<0.01	190-960	τ_1 = 3.3 ± 0.4 ns[f] (A_1 = 0.77) τ_2 = 6.7 ± 1.4 ns[f] (A_2 = 0.22)

[a] Emission maximum wavelengths. [b] Emission quantum yield. [c] Detecting wavelength. [d] Emission lifetime in each detection wavelength. [e] Pre-exponential factor. [f] Average of three single-crystals.

Supplementary Tables for X-ray Crystallography and DFT Calculation

Table S7 Crystal parameters and refinement data.

	1N	**1P**	**1P**•*c*-Hex (150 K)	**1P**•*c*-Hex (100 K)	**1P**•Paraffin
CCDC No.	2003915	2003916	2003917	2032282	2003918
Temperature (K)	150	150	150	100	150
Formula	$C_{19}H_{13}N_3O_2Pt$	$C_{19}H_{13}N_3O_2Pt{\cdot}{}^2/_3(H_2O)$	$C_{19}H_{13}N_3O_2Pt{\cdot}{}^1/_3(C_6H_{12})$	$C_{19}H_{13}N_3O_2Pt{\cdot}{}^1/_3(C_6H_{12})$	$C_{19}H_{13}N_3O_2Pt$ (+ solv.)
Crystal system	Monoclinic	Trigonal	Trigonal	Trigonal	Trigonal
Space group	$P2_1/c$ (#14)	$R\bar{3}$ (#148)	$R\bar{3}$ (#148)	$R\bar{3}$ (#148)	$R\bar{3}$ (#148)
a (Å)	11.0034(1)	30.4714(3)	30.2896(3)	30.2541(5)	30.402(2)
b (Å)	12.6502(1)	30.4714(3)	30.2896(3)	30.2541(5)	30.402(2)
c (Å)	23.9841(2)	10.0419(1)	10.0570(1)	10.0134(2)	10.0404(8)
α (deg)	90	90	90	90	90
β (deg)	98.435(1)	90	90	90	90
γ (deg)	90	120	120	120	120
V (Å^3)	3302.36(5)	8074.8(2)	7990.7(2)	7937.4(3)	8037(1)
Z	8	18	18	18	18
Reflns collected	24028	8439	8545	8283	12983
Unique reflns	5890	3188	3584	3517	3526
D_{calc} (g cm^{-1})	2.053	1.934	2.014	2.028	1.898
R_{int}	0.0293	0.0144	0.0193	0.0305	0.1143
R_1 ($I > 2\sigma(I)$)[a]	0.0258	0.0212	0.0259	0.0239	0.0719
wR_2[b]	0.0689	0.0582	0.0742	0.0634	0.1599
GOF	1.073	1.144	1.087	1.079	1.086

[a] $R_1 = \Sigma||F_o|-|F_c|| / \Sigma|F_o|$. [b] $wR_2 = [\Sigma w(F_o^2 - F_c^2)/ \Sigma w(F_o)^2]^{1/2}$, $w = [\sigma_c^2(F_o^2) + (xP)^2 + yP]^{-1}$, $P = (F_o^2 - 2F_c^2)/3$.

Table S8 Computed vertical excitations of the trimeric unit **1P**.

Excited State	1:	Singlet-A	2.8012 eV	442.60 nm	*f*=0.0443	<S**2>=0.000
273 -> 274		0.52241				
273 -> 275		0.41056				
273 -> 276		0.18748				
Excited State	2:	Singlet-A	2.8697 eV	432.04 nm	*f*=0.0013	<S**2>=0.000
267 -> 274		0.11573				
273 -> 274		-0.37729				
273 -> 275		0.54590				
273 -> 276		-0.13703				
Excited State	3:	Singlet-A	2.9014 eV	427.32 nm	*f*=0.0004	<S**2>=0.000
273 -> 274		-0.22240				
273 -> 276		0.64979				
Excited State	4:	Singlet-A	3.0807 eV	402.45 nm	*f*=0.0042	<S**2>=0.000
271 -> 275		0.22564				
271 -> 276		-0.11062				
272 -> 274		0.27353				
272 -> 275		0.57150				
Excited State	5:	Singlet-A	3.1370 eV	395.23 nm	*f*=0.0114	<S**2>=0.000
270 -> 274		0.31434				
270 -> 275		-0.14230				
271 -> 274		0.37323				
271 -> 275		0.18346				
271 -> 276		0.13422				
272 -> 274		-0.28373				
272 -> 276		-0.23466				
273 -> 277		-0.13095				
Excited State	6:	Singlet-A	3.1578 eV	392.63 nm	*f*=0.0021	<S**2>=0.000
270 -> 274		0.42072				
271 -> 275		-0.31272				
271 -> 276		-0.21182				
272 -> 275		0.13718				

(Continued)

272 -> 276	0.30460				
273 -> 277	-0.13761				
273 -> 278	0.13924				
Excited State 7:	Singlet-A	3.2084 eV	386.44 nm	*f*=0.0014	<S**2>=0.000
267 -> 277	-0.11803				
271 -> 274	0.11779				
272 -> 274	-0.11458				
273 -> 277	0.53449				
273 -> 278	0.36803				
Excited State 8:	Singlet-A	3.2229 eV	384.70 nm	*f*=0.0067	<S**2>=0.000
270 -> 274	-0.13727				
271 -> 275	0.17129				
272 -> 275	-0.10091				
273 -> 277	-0.34952				
273 -> 278	0.54124				
Excited State 9:	Singlet-A	3.2498 eV	381.51 nm	*f*=0.0023	<S**2>=0.000
270 -> 275	-0.12078				
271 -> 275	0.42314				
271 -> 276	-0.28749				
272 -> 275	-0.21756				
272 -> 276	0.33646				
273 -> 278	-0.14747				
Excited State 10:	Singlet-A	3.2789 eV	378.13 nm	*f*=0.0028	<S**2>=0.000
270 -> 274	0.37168				
270 -> 275	-0.11122				
271 -> 274	-0.24144				
271 -> 275	0.12769				
271 -> 276	0.14926				
272 -> 274	0.39375				
272 -> 275	-0.19553				
272 -> 276	-0.16966				
Excited State 11:	Singlet-A	3.3641 eV	368.55 nm	*f*=0.0072	<S**2>=0.000

(Continued)

267 -> 279	0.13191				
273 -> 279	0.67409				
Excited State 12:	Singlet-A	3.3948 eV	365.22 nm	*f*=0.0033	<S**2>=0.000
271 -> 274	0.29214				
271 -> 276	0.45593				
272 -> 274	0.22496				
272 -> 276	0.36147				
Excited State 13:	Singlet-A	3.4723 eV	357.07 nm	*f*=0.0041	<S**2>=0.000
271 -> 274	0.40941				
271 -> 275	-0.22539				
271 -> 276	-0.24980				
272 -> 274	0.32798				
272 -> 275	-0.17329				
272 -> 276	-0.19542				
272 -> 279	-0.12942				
Excited State 14:	Singlet-A	3.4858 eV	355.69 nm	*f*=0.0070	<S**2>=0.000
270 -> 274	0.10051				
270 -> 275	0.28655				
270 -> 276	0.56049				
271 -> 278	-0.13408				
272 -> 278	0.13763				
Excited State 15:	Singlet-A	3.5014 eV	354.10 nm	*f*=0.0064	<S**2>=0.000
269 -> 274	0.18672				
269 -> 275	0.23246				
270 -> 277	0.34686				
271 -> 277	0.18270				
271 -> 278	0.21021				
271 -> 279	-0.11981				
272 -> 277	-0.20962				
272 -> 278	-0.25745				
272 -> 279	-0.18135				
Excited State 16:	Singlet-A	3.5213 eV	352.09 nm	*f*=0.0255	<S**2>=0.000

(Continued)

268 -> 275	0.11738				
269 -> 275	-0.21007				
270 -> 276	-0.13045				
270 -> 277	0.38627				
271 -> 277	0.21790				
271 -> 279	0.17899				
272 -> 277	-0.12786				
272 -> 278	0.11964				
272 -> 279	0.29307				
Excited State 17:	Singlet-A	3.5308 eV	351.15 nm	*f*=0.0122	<S**2>=0.000
268 -> 274	0.11712				
269 -> 274	0.27899				
269 -> 275	0.31040				
270 -> 277	-0.11244				
271 -> 279	0.24957				
272 -> 279	0.38639				
Excited State 18:	Singlet-A	3.5486 eV	349.39 nm	*f*=0.0469	<S**2>=0.000
266 -> 274	-0.10190				
269 -> 274	0.13931				
269 -> 275	0.25978				
270 -> 276	-0.12527				
270 -> 278	0.12924				
271 -> 278	-0.33382				
272 -> 278	0.39066				
272 -> 279	-0.12285				
Excited State 19:	Singlet-A	3.5830 eV	346.04 nm	*f*=0.0227	<S**2>=0.000
265 -> 274	-0.13378				
267 -> 274	0.24580				
267 -> 275	-0.11941				
268 -> 274	0.31348				
269 -> 274	0.33211				
269 -> 275	-0.29170				
272 -> 277	-0.10276				
273 -> 274	0.10730				

(Continued)

Excited State 20:	Singlet-A	3.6349 eV	341.09 nm	*f*=0.0600	<S**2>=0.000
261 -> 274	-0.15886				
263 -> 275	0.17714				
266 -> 275	-0.11135				
267 -> 274	0.40493				
268 -> 274	-0.22212				
268 -> 275	-0.21929				
269 -> 274	-0.12860				
269 -> 276	-0.17300				
270 -> 277	0.10641				

References

S1 J. H. Price, A. N. Williamson, P. F. Schramm and B. B. Wayland, *Inorg. Chem.*, 1972, **11**, 1280-1284.

S2 *CrysAlisPro*, Rigaku Corporation, Tokyo, Japan, 2015.

S3 G. M. Sheldrick, *Acta Crystallogr., Sect. A*, 2015, **71**, 3-8.

S4 G. M. Sheldrick, *Acta Crystallogr., Sect. C*, 2015, **71**, 3-8.

S5 (a) P. van der Sluis and A. L. Spek, *Acta Crystallogr., Sect. A*, 1990, **46**, 194-201; (b) A. L. Spek, *Acta Crystallogr., Sect. A*, 1990, **46**, C34.

S6 A. L. Smirl, J. B. Clark, E. W. V. Stryland and B. R. Russell, *J. Chem. Phys.*, 1982, **77**, 631-640.

S7 (a) W. R. Dawson and M. W. Windsor, *J. Phys. Chem.*, 1968, **72**, 3251-3260; (b) W. H. Melhuish, *J. Phys. Chem.*, 1961, **65**, 229-235.

S8 (a) M. Ernzerhof and G. E. Scuseria, *J. Chem. Phys.*, 1999, **110**, 5029-5306; (b) C. Adamo and V. Barone, *J. Chem. Phys.*, 1999, **110**, 6158-6170.

S9 *Gaussian 09*, Revision D.01, M. J. Frisch, G. W. Trucks, H. B. Schlegel, G. E. Scuseria, M. A. Robb, J. R. Cheeseman, G. Scalmani, V. Barone, B. Mennucci, G. A. Petersson, H. Nakatsuji, M. Caricato, X. Li, H. P. Hratchian, A. F. Izmaylov, J. Bloino, G. Zheng, J. L. Sonnenberg, M. Hada, M. Ehara, K. Toyota, R. Fukuda, J. Hasegawa, M. Ishida, T. Nakajima, Y. Honda, O. Kitao, H. Nakai, T. Vreven, J. A. Montgomery, Jr., J. E. Peralta, F. Ogliaro, M. Bearpark, J. J. Heyd, E. Brothers, K. N. Kudin, V. N. Staroverov, T. Keith, R. Kobayashi, J. Normand, K. Raghavachari, A. Rendell, J. C. Burant, S. S. Iyengar, J. Tomasi, M. Cossi, N. Rega, J. M. Millam, M. Klene, J. E. Knox, J. B. Cross, V. Bakken, C. Adamo, J. Jaramillo, R. Gomperts, R. E. Stratmann, O. Yazyev, A. J. Austin, R. Cammi, C. Pomelli, J. W. Ochterski, R. L. Martin, K. Morokuma, V. G. Zakrzewski, G. A. Voth, P. Salvador, J. J. Dannenberg, S. Dapprich, A. D. Daniels, O. Farkas, J. B. Foresman, J. V. Ortiz, J. Cioslowski and D. J. Fox, Gaussian, Inc., Wallingford CT, 2013.

S10 D. Andrae, U. Häussermann, M. Dolg, H. Stoll and H. Preuss, *Theor. Chim. Acta*, 1990, **77**, 123-141.

S11 (a) R. Ditchfield, W. J. Hehre and J. A. Pople, *J. Chem. Phys.*, 1971, **54**, 724-728; (b) W. J. Hehre, R. Ditchfield and J. A. Pople, *J. Chem. Phys.*, 1972, **56**, 2257-2261; (c) P. C. Hariharan and J. A. Pople, *Theor. Chim. Acta*, 1973, **28**, 213-222.

S12 (a) A. K. Mishra and S. K. Dogra, *Spectrochim. Acta A*, 1983, **39**, 609-611; b) J. J. Inbaraj, P. Bilski and C. F. Chignell, *Photochem. Photobiol.*, 2002, **75**, 107-116.

S13 (a) V. M. Miskowski, V. H. Houlding, C.-M. Che and Y. Wang, *Inorg. Chem.*, 1993, **32**, 2518-2524; (b) M. Kato, C. Kosuge, K. Morii, J. S. Ahn, H. Kitagawa, T. Mitani, M. Matsushita, T. Kato, S. Yano and M. Kimura, *Inorg. Chem.*, 1999, **38**, 1638-1641; (c) Y. Shigeta, A. Kobayashi, T. Ohba, M. Yoshida, T. Matsumoto, H.-C. Chang and M. Kato, *Chem. Eur. J.*, 2016, **22**, 2682-2690; (d) M. Nakagaki, S. Aono, M. Kato and S. Sakaki, *J.*

Phys. Chem. C, 2020, **124**, 10453-10461.

S14 *TOPAS v4.2*, general profile and structure analysis software for powder diffraction data. Bruker AXS, Karlsruhe, Germany, **2011**.

S15 (a) H. Li, J. Ding, Z. Xie, Y. Cheng and L. Wang, *J. Organomet. Chem.*, 2009, **694**, 2777-2785; (b) P.-H. Lanoë, A. Moreno-Betancourt, L. Wilson, C. Philouze, C. Monnereau, H. Jamet, D. Jouvenot and F. Loiseau, *Dyes and Pigments*, 2019, **162**, 967-977.

S16 J. Gao, S. Wu and M. A. Rogers, *J. Mater. Chem.*, 2012, **22**, 12651-12658.

S17 H. Iino, M. Fujii, M. Fujino, S. Kohara, K. Hashizaki, H. Kira, N. Koizumi, Y. Watanabe and N. Utoguchi, *Biol. Pharm. Bull.*, 2017, **40**, 220-226.